

Relaxation of Single Electron Spins by Nuclei in a Double Quantum Dot

A. C. Johnson¹, J. R. Petta¹, J. M. Taylor¹, A. Yacoby^{1,2}, M. D. Lukin¹, C. M. Marcus¹,
M. P. Hanson³, A. C. Gossard³

¹ *Department of Physics, Harvard University, Cambridge, Massachusetts 02138, USA*

² *Department of Condensed Matter Physics, Weizmann Institute of Science, Rehovot 76100, Israel*

³ *Materials Department, University of California, Santa Barbara, California 93106, USA*

The spin of a confined electron, when oriented originally in some direction, will lose memory of that orientation after some time. Physical mechanisms leading to this relaxation of spin memory typically involve either coupling of the electron spin to its orbital motion or to nuclear spins¹⁻⁷. Relaxation of confined electron spin has been previously measured only for Zeeman or exchange split spin states, where spin-orbit effects dominate relaxation⁸⁻¹⁰, while relaxation due to nuclei has been observed in optical spectroscopy studies¹¹. Using an isolated GaAs double quantum dot defined by electrostatic gates and direct time domain measurements, we investigate in detail spin relaxation for arbitrary splitting of spin states. Results demonstrate that the relaxation time is dominated by nuclear interactions and increases by several orders of magnitude when a magnetic field of a few millitesla is applied. These results have significant implications for spin-based information processing¹².

The coupling of nuclear spins to electrons in low-dimensional semiconductors is known from optical and transport studies in quantum Hall systems to yield rich physical effects and provide new probes of the relatively isolated quantum system of nuclear spins in solids¹³⁻¹⁶. Confined electrons interacting with relatively few nuclei are particularly sensitive to hyperfine coupling. This can lead to dramatic effects such as tunnelling currents that slowly oscillate in time^{17,18}, and electrical control and readout of nuclear polarization¹⁹. Here, we show that the interaction between single electrons confined in quantum dots with ensembles of lattice nuclei can dominate electron spin relaxation.

We use high-frequency pulsed gates to measure spin relaxation in a GaAs double quantum dot (Fig. 1a). Measurements are performed near the (1,1) to (0,2) charge transition, where (n,m) denotes the absolute number of electrons on the left and right dots. In the (0,2) configuration, the two electrons form a spin singlet to avoid the large Pauli exclusion energy cost ($0.4 \text{ meV} \gg kT \sim 10 \text{ \mu eV}$) of occupying an excited orbital state^{20,21}. In the separated (1,1) configuration, the two electrons may occupy any spin state. That is, apart from any Zeeman energy ($\sim 2.5 \text{ \mu eV}$ at 100 mT), the singlet, (1,1)S, and three triplets, (1,1)T₋, (1,1)T₀, and (1,1)T₊ ($m_s = -1, 0, 1$ respectively) are effectively degenerate given the weak interdot coupling to which the system is tuned.

Spin relaxation is measured by preparing an unpolarized mixture of (1,1) states and monitoring the probability of transition to (0,2)S after the latter is made lower in energy by changing the electrostatic gate configuration. The different local environments acting on the two spins cause the two-electron spin state to evolve in time, and only if this spin state passes near (1,1)S is a transition to (0,2)S allowed. The average occupancy of the left dot, which reflects the probability of this transition, is monitored using local quantum point contact (QPC) charge sensors²⁰. Conductances g_{ls} and g_{rs} of the left and right sensors change by several percent when an electron enters the dot nearest the sensor²²⁻²⁵.

Energy levels of each dot were controlled by voltage pulses on gates L and R, as shown in Fig. 1c²⁰. The double dot was cycled through three configurations, depicted in Fig. 1e, while measuring the average QPC conductances. In the Empty (“E”) step, the second electron is removed, leaving a (0,1) state. In the Reset (“R”) step, a new second electron is added, initializing the (1,1) state to an unbiased mixture of the singlet, (1,1)S, and the three triplets (1,1)T₋, (1,1)T₀, and (1,1)T₊. In the Measurement (“M”) step, (0,2) is lowered relative to (1,1) until (0,2)S becomes the ground state, while the (0,2) triplets remain inaccessible, above the (1,1) states. Because tunnelling preserves spin, only (1,1)S can relax to (0,2)S, while the (1,1) triplets are spin-blockaded from making this transition^{26,27}.

The measurement step accounted for 80% of the pulse period (E and R were each 10%) so the time-averaged charge-sensor signal mainly reflects the charge state during the measurement time, t_M . Figure 1d shows g_{rs} as a function of the dc gate voltages V_L and V_R with pulses applied. The dashed lines indicate locations of ground-state transitions during the M step, as seen in unperturbed double dots²³. Gate pulses alter this signal only within the “pulse triangle” (outlined by solid white lines). Here g_{rs} is intermediate between the (0,2) and (1,1) plateaus, indicating that although (0,2) is the ground state, the system is often stuck in the excited (1,1) state. In the regions labelled M' and M'', alternate, spin-independent relaxation pathways, shown in Fig. 1f, circumvent the spin blockade.

The magnetic field, B , and t_M dependence of the charge sensor signal is shown in Fig. 2. With $t_M = 8 \mu\text{s}$, a large signal is seen in the pulse triangle indicating that some of the (1,1) to (0,2) transitions are spin blocked. As t_M is increased this signal decreases (Fig. 2b), indicating that t_M is approaching the (1,1) singlet-triplet relaxation time. This is accompanied by a reduction in the pulse triangle size due to thermally activated processes as in Fig. 1f. Similar data, but at $B = 0$, are plotted in Figs. 2c,d. The signal in

the pulse triangle is noticeably weaker for the same t_M , particularly near the (1,1) to (0,2) charge transition, indicating enhanced spin relaxation.

Detailed measurements of residual (1,1) occupation as a function of detuning (the energy difference between the (1,1) and (0,2) states) are shown in Fig. 3. Conductances g_{ls} and g_{rs} were measured along the diagonal white line in the upper panel of Fig. 3, for various B and t_M , and converted to occupation, $\langle N \rangle$, by scaling to the average (1,1) and (0,2) levels outside the pulse triangle. Data are shown in detail for the points labelled A through D. As in Fig. 2, strong field dependence was found at low detuning (point A) where inelastic interdot tunnelling dominates. This field dependence vanishes at higher detuning where thermally activated tunnelling to the leads dominates.

As in previous work^{4,11}, we model spin evolution in (1,1) by treating the ensemble of nuclear spins within each dot as a static effective field \mathbf{B}_{nuc} with slow internal dynamics, that adds to any applied Zeeman field (see Fig. 1b). \mathbf{B}_{nuc} is randomly oriented with rms strength $B_{nuc} = b_0 \sqrt{I_0(I_0 + 1)/N_{nuc}}$, where $b_0 = 3.5$ T is the hyperfine constant in GaAs, $I_0 = 3/2$ is the nuclear spin and N_{nuc} is the effective number of nuclei with which the electron interacts^{2,3,28,29}. In our dots, N_{nuc} is estimated at $10^6 - 10^7$, giving $B_{nuc} \sim 2 - 6$ mT. The spins precess in a characteristic time $t_{nuc} = \hbar/g^* \mu_B B_{nuc} \sim 3 - 10$ ns, which can be regarded as an inhomogeneous dephasing time T_2^* . At $B = 0$, all four (1,1) spin states mix in this time, and tunnelling will appear insensitive to spin. With $B > B_{nuc}$ however, only (1,1)T₀ and (1,1)S are degenerate. These will continue to mix with the same rate, but (1,1)T₊ and T₋ will be frozen out.

To model this mixing, we assume static nuclear fields during each pulse, a spin-preserving inelastic interdot tunnelling rate Γ_{in} from (1,1)S to (0,2)S, and a spin-independent rate Γ_T due to thermally activated tunnelling via the (0,1) and (1,2) charge states. Zeeman eigenstates for two spins in fields $B \hat{\mathbf{z}} + \mathbf{B}_{nuc,l}$ and $B \hat{\mathbf{z}} + \mathbf{B}_{nuc,r}$, denoted $|(1,1)s,s'\rangle$ ($s,s'=\pm 1/2$), decay to (0,2)S based on their overlap with (1,1)S, with rates

$\Gamma_{s,s'} = \Gamma_{in} \langle (1,1)S | (1,1)s, s' \rangle^2$ as long as $\Gamma_{in} \ll g^* \mu_B B_{nuc}$. Averaging over nuclear field configuration and short-time dynamics gives decay rates for the T_{\pm} -like states

$$\Gamma_{\pm 1/2, \pm 1/2} = \frac{\Gamma_{in}}{4(1 + (B/B_{nuc})^2)} \quad (1)$$

and $\Gamma_{\pm 1/2, \mp 1/2} = \Gamma_{in}/2 - \Gamma_{\pm 1/2, \pm 1/2}$ for the S-like and T_0 -like states. At $B = 0$, total transition rates for all $(1,1)$ states into $(0,2)S$ are the same, $\tau_0^{-1} = \Gamma_{in}/4 + \Gamma_T$. For $B > B_{nuc}$, transitions rates $\tau_B^{-1} = \Gamma_{\pm 1/2, \pm 1/2} + \Gamma_T$ from $(1,1)T_{\pm}$ to $(0,2)S$ are suppressed by field, while transitions from $(1,1)S$ and $(1,1)T_0$ to $(0,2)S$ are accelerated by up to a factor of two because they no longer mix with $(1,1)T_{\pm}$. During the gate-pulse transition from R to M, the relatively fast transition from $(1,1)S$ to $(0,2)S$ allows a fraction q of the $(1,1)S$ state to transfer adiabatically to $(0,2)S$, reducing the initial occupation of $(1,1)S$. The resulting average occupancy N of $(1,1)$ after a time t_M is

$$N(t_M) = \frac{1}{t_M} \int_0^{t_M} dt \left(\frac{1}{2} e^{-t/\tau_B} + \frac{2-q}{4} e^{-t(2\tau_0^{-1} - \tau_B^{-1})} \right) \quad (2)$$

Experimentally measured values for N as functions of t_M and B for various detunings are shown in Fig. 3, along with fits to the above theory. An additional field-independent parameter, N_{∞} , accounts for nonzero $N(t_M)$ at long times due to thermal occupation of $(1,1)$. $N_{\infty} = 0$ at large detuning but increases, as expected, near zero detuning. Nonzero q values are found only at very low and very high detuning (where the R point is near zero detuning), where the slew rate of the pulse is low as it crosses to $(0,2)$. With these parameters and τ_0 set for a given detuning by fitting the zero field data (red), the high-field data (blue) are fit with just the longer decay times τ_B for the $(1,1)T_{\pm}$ states. The field-dependence curves (black) are then fully determined by B_{nuc} , which is most accurately determined from data in Fig. 4, as discussed below. Drift in sensor conductance over long field sweeps is compensated by allowing a vertical shift in the

field-dependence curves. The depth and width of the dips in these curves is not adjustable.

Figure 4 shows the extracted decay times τ_0 and τ_B versus detuning for various fields. As field increases, more points at high detuning fall along a line in this semi-log plot, denoting exponential energy dependence as expected for a thermally activated process. This persists over three orders of magnitude at the highest field, and with calibration from transport measurements yields a temperature of 160 ± 20 mK. At zero field, thermal decay dominates only at the highest detunings, and the low-detuning times are well fit by a power law function of detuning with exponent 1.2 ± 0.2 and offset 700 ns, typical of inelastic tunnelling in double quantum dots³⁰. Adding these two processes gives the red curve in Fig. 4, in good agreement with the zero-field data. The 10 mT curve is fit using these zero-field parameters, but with times for the inelastic component increased by the factor $(1 + (B/B_{nuc})^2)$ from equation (1). The fit gives $B_{nuc}=2.8\pm0.2$ mT, or $N_{nuc} \sim 6 \times 10^6$, within expectations. This value uniquely determines the remaining theory curves. For τ_B longer than about 1 ms the decay is faster than theory predicts (though still 10^3 times slower than at $B=0$), indicating that another mechanism such as spin-orbit coupling may operate on millisecond time scales⁸⁻¹⁰. Given B_{nuc} above, the model predicts $T_2^* \sim 9$ ns for this device. For times longer than this, up to 1 ms, the excellent agreement between experiment and theory indicates that hyperfine interaction is the only relevant source of spin relaxation in this system.

References

1. Khaetskii, A. V., Nazarov, Y. V. Spin relaxation in semiconductor quantum dots. *Phys. Rev. B* **61**, 12639 (2000).
2. Erlingsson, S. I., Nazarov, Y. V., Fal'ko V. I. Nucleus-mediated spin-flip transitions in GaAs quantum dots. *Phys. Rev. B* **64** 195306 (2001).

3. Khaetskii, A. V., Loss, D., Glazman, L. Electron spin decoherence in quantum dots due to interaction with nuclei. *Phys. Rev. Lett.* **88**, 186802 (2002).
4. Merkulov, I. A., Efros, Al. L., Rosen, M. Electron spin relaxation by nuclei in semiconductor quantum dots. *Phys. Rev. B* **65**, 205309 (2002).
5. de Sousa, R., Das Sarma, S. Theory of nuclear-induced spectral diffusion: Spin decoherence of phosphorus donors in Si and GaAs quantum dots. *Phys. Rev. B* **68**, 115322 (2003).
6. Coish, W. A., Loss, D. Hyperfine interaction in a quantum dot: Non-Markovian electron spin dynamics. *Phys. Rev. B* **70**, 195340 (2004).
7. Golovach, V. N., Khaetskii, A., Loss, D. Phonon-induced decay of the electron spin in quantum dots. *Phys. Rev. Lett.* **93**, 016601 (2004).
8. Fujisawa, T., Austing, D. G., Tokura, Y., Hirayama, Y., Tarucha, S. Allowed and forbidden transitions in artificial hydrogen and helium atoms. *Nature* **419**, 278 (2002).
9. Elzerman, J. M. et al. Single-shot readout of an individual electron spin in a quantum dot. *Nature* **430**, 431 (2004).
10. Kroutvar M. et al. Optically programmable electron spin memory using semiconductor quantum dots. *Nature* **432**, 81 (2004).
11. Bracker, A. S. et al. Optical pumping of the electronic and nuclear spin of single charge-tunable quantum dots. *Phys. Rev. Lett.* **94**, 047402 (2005).
12. Loss, D., DiVincenzo, D. P. Quantum computation with quantum dots. *Phys. Rev. A* **57**, 120 (1998).
13. Wald, K. R., Kouwenhoven, L. P., McEuen, P. L., Van der Vaart, N. C., Foxon, C. T. Local dynamic nuclear polarization using quantum point contacts. *Phys. Rev. Lett.* **73**, 1011 (1994).

14. Salis, G. Optical manipulation of nuclear spin by a two-dimensional electron gas. *Phys. Rev. Lett.* **86**, 2677 (2001).
15. Kumada, N., Muraki, K., Hashimoto, K., Hirayama, Y. Spin degree of freedom in the $v=1$ bilayer electron system investigated via nuclear spin relaxation. Preprint at <<http://arxiv.org/abs/cond-mat/0410495>> (2004).
16. Smet, J. H., Deutschmann, R. A., Ertl, F., Wegscheider, W., Abstreiter, G., von Klitzing, K. Gate-voltage control of spin interactions between electrons and nuclei in a semiconductor. *Nature* **415**, 281 (2002).
17. Ono, K., Tarucha, S. Nuclear-spin-induced oscillatory current in spin-blockaded quantum dots. *Phys. Rev. Lett.* **92**, 256803 (2004).
18. Bracker, A. S. et al. Optical pumping of the electronic and nuclear spin of single charge-tunable quantum dots. *Phys. Rev. Lett.* **94**, 047402 (2005).
19. Ono, K., and Tarucha, S. et al. *unpublished*.
20. Petta, J. R. et al. Pulsed gate measurements of the singlet-triplet relaxation time in a two-electron double quantum dot. Preprint at <<http://arxiv.org/abs/cond-mat/0412048>> (2004).
21. Ashoori, R. C. et al. N-electron ground-state energies of a quantum-dot in a magnetic field. *Phys. Rev. Lett.* **71**, 613 (1993).
22. Field, M. et al. Measurements of Coulomb blockade with a non-invasive voltage probe. *Phys. Rev. Lett.* **70**, 1311 (1993).
23. DiCarlo, L. et al. Differential Charge Sensing and Charge Delocalization in a Tunable Double Quantum Dot. *Phys. Rev. Lett.* **92**, 226801 (2004).
24. Elzerman, J. M. et al. Few-electron quantum dot circuit with integrated charge readout. *Phys. Rev. B* **67**, 161308 (2003).

25. Petta J. R., Johnson A. C., Marcus, C. M., Hanson, M. P., Gossard, A. C. Manipulation of a single charge in a double quantum dot. *Phys. Rev. Lett.* **93**, 186802 (2004).

26. Ono, K., Austing, D. G., Tokura, Y., Tarucha, S. Current rectification by Pauli exclusion in a weakly coupled double quantum dot system. *Science* **297**, 1313 (2002).

27. Johnson, A. C., Petta J. R., Marcus, C. M., Hanson, M. P., Gossard, A. C. Singlet-triplet spin blockade and charge sensing in a few-electron double quantum dot. Preprint at <<http://arxiv.org/abs/cond-mat/0410679>> (2004).

28. Paget, D., Lampel, G., Sapoval, B., Safarov, V. I. Low field electron-nuclear spin coupling in gallium-arsenide under optical-pumping conditions. *Phys. Rev. B* **15**, 5780 (1977).

29. Dobers, M., von Klitzing, K., Schneider, J., Weimann, G., Ploog, K. Electrical detection of nuclear magnetic-resonance in GaAs-Al_xGa_{1-x}As heterostructures. *Phys. Rev. Lett.* **61**, 1650 (1988).

30. Fujisawa, T. et al. Spontaneous emission spectrum in double quantum dot devices. *Science* **282**, 932 (1998).

Acknowledgements We thank H.A. Engel and Peter Zoller for useful discussions. This work was supported by the ARO under DAAD55-98-1-0270 and DAAD19-02-1-0070, the DARPA-QuIST programme, and the NSF under DMR-0072777 and the Harvard NSEC.

Correspondence and requests for materials should be addressed to C.M. (e-mail: marcus@harvard.edu).

Figure 1 Measuring spin-selective tunnelling in a double quantum dot. **a**, Scanning electron micrograph of a device similar to the one measured. Metallic gates deplete a two-dimensional electron gas 100 nm below the surface, with density $2 \times 10^{11} \text{ cm}^{-2}$. A double dot is defined between gates L and R. Electrons can tunnel weakly between the dots and to conducting leads. The conductances g_{ls} and g_{rs} of the left and right quantum point contacts (QPCs) reflect the average occupation of each dot. **b**, Schematic of the (1,1) charge configuration. The spatially separated electrons feel different effective fields due to hyperfine interaction with the local Ga and As nuclei, in addition to a uniform externally applied field. **c**, Voltage pulses applied to gates L and R cycle through three configurations, Empty (E), Reset (R) and Measure (M). **d**, Right sensor conductance g_{rs} as a function of dc voltages on the same two gates around the (1,1) to (0,2) transition, with cyclical displacements by the pulses shown by points E, R, and M. The dashed lines outline sensor plateaus indicating the stable charge configurations (0,1), (1,1), (0,2), and (1,2) during the M step. Inside the solid white-outlined “pulse triangle,” the ground state is (0,2), but higher sensor conductance indicates that tunnelling is partially spin blocked. A plane is subtracted from the raw data to remove direct gate-QPC coupling. **e**, Energetics of the pulse sequence. In (0,2), only the singlet (0,2)S is accessible, whereas in (1,1), singlet and triplet are degenerate. (0,1) and (1,2) are both spin-1/2 doublets. Step E empties the second electron, leaving one electron in the right dot. Step R loads an electron into the left dot, occupying all four (1,1) states with equal probability. At M, (0,2)S is the ground state, but as tunnelling preserves spin, only (1,1)S and the $m_s=0$ triplet (1,1)T₀, with which it quickly mixes, can tunnel. Mixing of (1,1)T₊ and (1,1)T₋ with the singlet is weak away from zero field, hence their tunnelling is blocked. **f**, Energetics outside the pulse triangle. Below the pulse triangle, labelled M', the one-electron state (0,1) has lower energy than (1,1) and provides an alternate, spin-independent path to (0,2). Above the pulse triangle, labelled M'', the three-electron state (1,2) provides an alternate spin-independent path.

Figure 2 Dependence of the occupancy of the (1,1) state on measurement time, t_M , and external field, B . **a**, Charge sensor conductance, g_{rs} , as a function of V_L and V_R with short pulses ($t_M = 8 \mu\text{s}$) at $B=100 \text{ mT}$. Large average occupation of (1,1) is seen throughout the pulse triangle. Near the triangle edges, thermally activated tunnelling to the leads allows fast relaxation to (0,2), (see Fig. 1f). **b**, For longer pulses ($t_M = 80 \mu\text{s}$), thermally relaxed triangle edges expand toward the centre of the triangle. **c**, At $B=0$, the (1,1) occupation is extinguished at low-detuning (near the (1,1)-(0,2) charge transition) as tunnelling to (0,2) becomes possible from the (1,1) T_+ and (1,1) T_- states. **d**, Combine these two effects at zero field with long pulses, and no residual (1,1) occupation is seen, indicating complete relaxation to (0,2).

Figure 3 Detailed measurements of blockaded (1,1) occupation. Average occupation $\langle N \rangle$ of the (1,1) charge state, based on calibrated charge sensor conductances, at four detuning points (labelled A, B, C, D on the upper graph). Left panels show $\langle N \rangle$ as a function of t_M at $B = 0$ and $B = 150 \text{ mT}$. Middle panels show $\langle N \rangle$ as a function of B for different t_m times. Diagrams at right show schematically the relative position of energy levels and the extracted ratios of inelastic (Γ_{in}) to thermal (Γ_T) decay rates.

Figure 4 Decay of (1,1) occupancy as a function of detuning at various magnetic fields. Dotted lines mark the locations of points A through D from Fig. 3. Fit of zero field theory (red curve) to data (red circles) sets all fit parameters except B_{nuc} , which is determined by fitting to the 10mT data (gold). Theory curves at other fields are then fully determined. Error bars at zero field result from the least squares fitting. Error bars at nonzero field reflect changes in the resulting decay rate as the zero-field fit parameters are varied within their uncertainties.

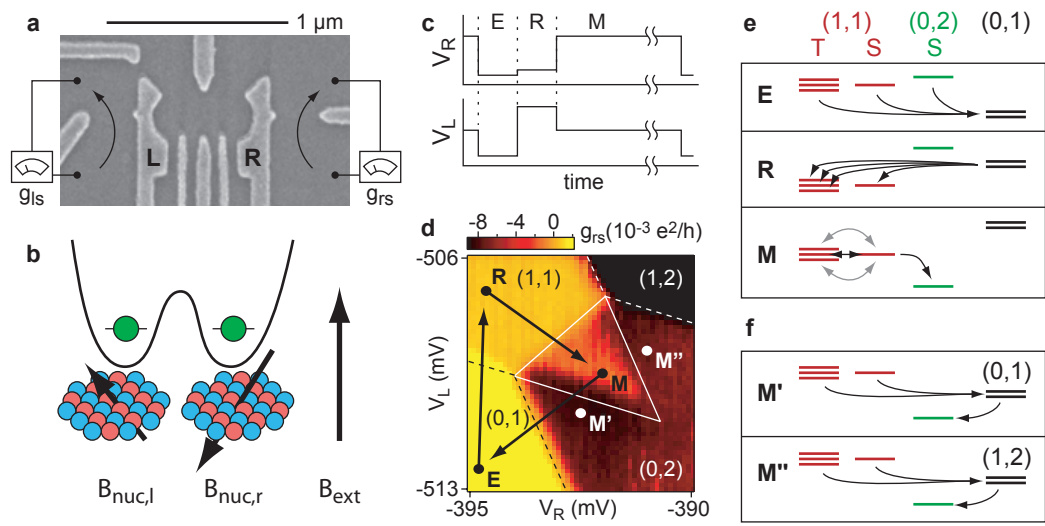


Figure 1

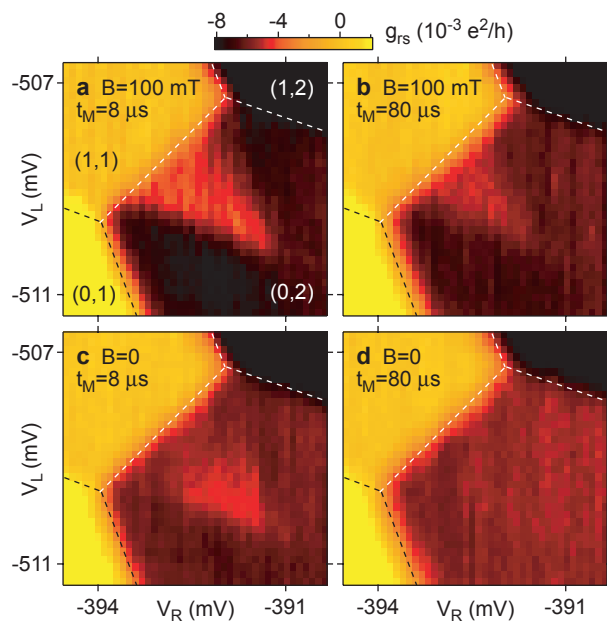


Figure 2

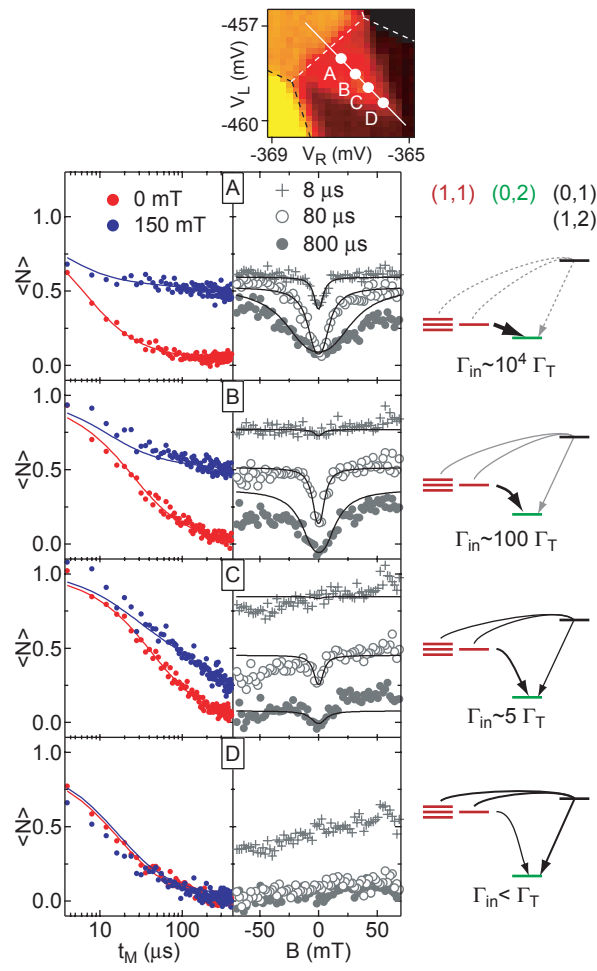


Figure 3

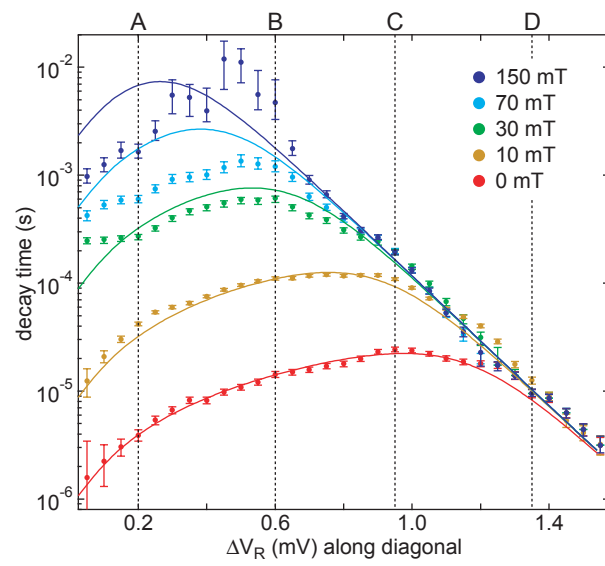


Figure 4